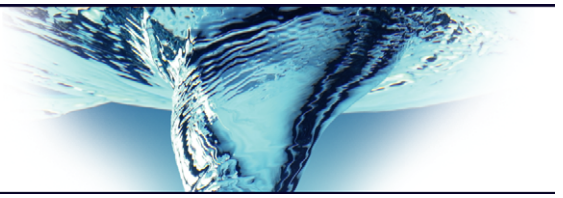
J. Fluid Mech. (2013), *vol.* 729, R2, doi:10.1017/jfm.2013.325



JFM RAPIDS
journals.cambridge.org/rapids

Bounds for Euler from vorticity moments and line divergence

Robert M. Kerr†

Department of Mathematics, University of Warwick, Coventry CV4 7AL, UK

(Received 6 January 2013; revised 11 June 2013; accepted 19 June 2013;
first published online 24 July 2013)

The inviscid growth of a range of vorticity moments is compared using Euler calculations of anti-parallel vortices with a new initial condition. The primary goal is to understand the role of nonlinearity in the generation of a new hierarchy of rescaled vorticity moments in Navier–Stokes calculations where the rescaled moments obey $D_m \geqslant D_{m+1}$, the reverse of the usual $\Omega_{m+1} \geqslant \Omega_m$ Hölder ordering of the original moments. Two temporal phases have been identified for the Euler calculations. In the first phase the $1 < m < \infty$ vorticity moments are ordered in a manner consistent with the new Navier–Stokes hierarchy and grow in a manner that skirts the lower edge of possible singular growth with $D_m^2 \to \sup|\boldsymbol{\omega}| \sim A_m(T_c - t)^{-1}$ where the A_m are nearly independent of m. In the second phase, the new D_m ordering breaks down as the Ω_m converge towards the same super-exponential growth for all m. The transition is identified using new inequalities for the upper bounds for the $-\mathrm{d}D_m^{-2}/\mathrm{d}t$ that are based solely upon the ratios D_{m+1}/D_m, and the convergent super-exponential growth is shown by plotting $\log(\mathrm{d}\log\Omega_m/\mathrm{d}t)$. Three-dimensional graphics show significant divergence of the vortex lines during the second phase, which could be what inhibits the initial power-law growth.

Key words: mathematical foundations, Navier–Stokes equations, vortex interactions

1. Background

Two unresolved issues that have limited the application of numerics to the vortex dynamics and regularity questions of the three-dimensional Euler equations have been the inadequate analysis tools and the difficulties in specifying reproducible initial conditions. The existing analysis tools are unable to simultaneously cover the necessary range of scales in both space and time, while existing methods for mapping vortex tubes onto Eulerian meshes tend to generate ghost images unless *ad hoc* massaging is applied (Bustamante & Kerr 2008; Hou 2008). This has led to weak and conflicting conclusions that depend upon the numerical method used and the choice of analysis that is applied to the results. To address these problems, this paper introduces

† Email address for correspondence: R.M.Kerr@warwick.ac.uk

© Cambridge University Press 2013

https://doi.org/10.1017/jfm.2013.325 Published online by Cambridge University Press

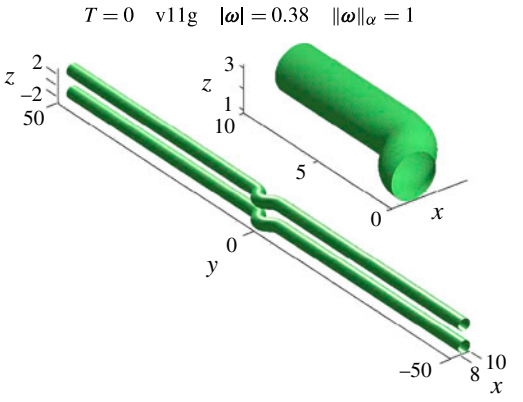


FIGURE 1. Very long, anti-parallel initial condition at $t = 0$. Their widths are $r \approx 1$ and the distances from their cores to the $z = 0$ dividing plane are $d = 1.5$. This is from case v11g in table 1.

an improved initialization for curved vortex tubes following an arbitrary trajectory and new analysis that is based upon higher-order vorticity moments, and then applies these to simulations of interacting anti-parallel vortices. The new vorticity profile (figure 1) suppresses core instabilities and the trajectory algorithm allows the evolution of vortices with the same local perturbation, but different lengths, to be compared. The new analysis is to compare all orders of the vorticity moments and their growth using both old and new bounds, which leads to more robust conclusions. Included is analysis that adapts a rescaling of the vorticity moments for the viscous Navier–Stokes equations (Gibbon 2012, 2013) to the inviscid Euler equations by converting the standard Ω_m, or L^{2m}, vorticity moments, into the following D_m moments:

$$D_m = (\varpi_0^{-1}\Omega_m)^{\alpha_m} \quad \text{where } \Omega_m = \left(L^{-3} \int_{\mathscr{V}} |\boldsymbol{\omega}|^{2m} \, \mathrm{d}V \right)^{1/2m}. \tag{1.1}$$

The choices for the frequency scale ϖ_0 are $\varpi_0 = \varpi_\nu = \nu/\mathsf{L}^2$ for the Navier–Stokes calculation and $\varpi_0 = \varpi_\Gamma = \nu/\mathsf{L}^2$ for the Euler calculations, using for L the largest length of the problem. Together with the exponents $\alpha_m = 2m/(4m-3)$, the new D_m help simplify the time-derivative inequalities of the vorticity moments.

The paper is organized as follows. First, the re-scaling of the vorticity moments D_m for the Navier–Stokes and Euler equations is discussed and an application of the D_m to a new Navier–Stokes reconnection calculation is used to introduce the new moment hierarchy. Next, the numerical method is stated and the new initial condition is described. Results for the $D_m(t)$ from the new Euler calculations are split into two phases. In the first phase the new D_m hierarchy forms even when viscosity is absent, along with signs that the hierarchy is beginning to break down. Next, new time-derivative analysis and a new bound upon the nonlinear terms are introduced in order to characterize the transition. Comparing these terms shows how the new hierarchy begins, then breaks down. In the second phase, the logarithms of the logarithmic time derivatives of the Ω_m are used to show that all the Ω_m are converging towards the same super-exponential growth rate. Finally, the physical space vorticity is viewed using both isosurfaces and vortex lines, which diverge significantly at the same time as the Ω_m are becoming super-exponential.

https://doi.org/10.1017/jfm.2013.325 Published online by Cambridge University Press

2. Vorticity moments: rescaling and time derivatives

Historically, the two limiting Ω_m ($m = 1$ and $m = \infty$) have been the basis of most bounds that address regularity questions. In the new language $\Omega_1^2 = Z = \varpi_0^2 D_1$, and the pointwise maximum of vorticity becomes $\Omega_\infty = \|\boldsymbol{\omega}\|_\infty = \varpi_0 D_\infty^2$. Doering (2009) discusses some additional applications of the Ω_m to Navier–Stokes regularity bounds.

Most of what is known about bounds for possible singularities of the Euler equations are results that come from the time integral of $\|\boldsymbol{\omega}\|_\infty$ and its extensions. That is, if

$$\int_0^t \|\boldsymbol{\omega}\|_\infty \,\mathrm{d}\tau < \infty \quad \text{for all time } t > 0, \tag{2.1}$$

then the Euler equations are regular (Beale, Kato & Majda 1984). We also know from Hölder inequalities that $\Omega_{m+1} \geqslant \Omega_m$ for all m.

The following expressions will be used:

$$Z = \Omega_1^2 \sim D_1, \quad L^{-3}\frac{\mathrm{d}}{\mathrm{d}t}\Omega_m^{2m} = 2m\int \mathrm{d}V \boldsymbol{\omega}\cdot\boldsymbol{S}\cdot\boldsymbol{\omega}|\boldsymbol{\omega}|^{2(m-1)} \quad \text{and} \quad Z_p = \frac{\mathrm{d}}{\mathrm{d}t}Z = \frac{\mathrm{d}}{\mathrm{d}t}\Omega_1^2, \tag{2.2}$$

where Z is the global mean square vorticity or enstrophy, Z_p is the nonlinear production of enstrophy, and $S_{ij} = 0.5(\partial u_i/\partial x_j + \partial u_j/\partial x_i)$ is the strain.

2.1. *Applying the D_m to numerical data*

Recently, Yeung, Donzis & Sreenivasan (2012) found that convergent statistics for their forced Navier–Stokes simulations can be obtained by taking ratios of the higher-order moments. Coincidentally, new mathematics (Gibbon 2012) has concluded that rescaled D_m (1.1) are the natural variables to use when expressing these ratios in inequalities of the time derivatives of the higher-order vorticity moments. Taken together, these two results could explain why it has been so difficult to obtain time averages of the higher-order vorticity and strain moments (Kerr 2012).

To demonstrate the usefulness of the Navier–Stokes $D_m(t)$ in numerical analysis, figure 2 shows their evolution using data from a viscous, anti-parallel reconnection calculation using initial condition v11g from table 1. The unexpected result is that the lower-order D_m bound the higher-order D_m for all times. This becomes stronger as m increases. Two new related papers are Kerr (2013), which shows the details of the physical space structures responsible for the $D_m(t)$ fluctuations in figure 2, and Donzis *et al.* (2013), which shows that this hierarchy is found for all the Navier–Stokes simulations it has been tested on, including forced and decaying isotropic calculations.

To adapt this rescaling to vorticity moments of the inviscid Euler equations, a non-viscous replacement for the scaling frequency ϖ_0 in (1.1) is needed. The inviscid modification chosen defines ϖ_0 with the circulation of the vortices Γ instead of the viscosity ν. This is inspired by an empirical guess used in the analysis of enstrophy growth in Bustamante & Kerr (2008) and gives $\varpi_0 = \varpi_\Gamma = \Gamma/\mathsf{L}^2$, with the choice $\mathsf{L} = 2L_y$, the size of the full periodic domain, for the primary calculation analysed.

For $m < \infty$, one computational advantage of using these inviscid D_m in numerical analysis of the Euler equations is that they and their time derivatives $\mathrm{d}D_m/\mathrm{d}t$ can be determined at run-time, using the $\mathrm{d}\Omega_m/\mathrm{d}t$ from (2.2). These can then be compared against new bounds suggested by mathematical analysis or suggested types of growth such as power laws or super-exponential.

https://doi.org/10.1017/jfm.2013.325 Published online by Cambridge University Press

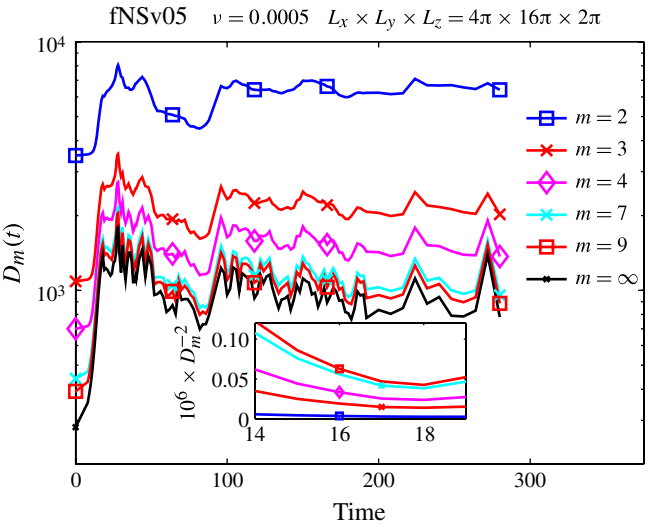


FIGURE 2. Navier–Stokes $m > 1 D_m$ (1.1) from a $Re = \Gamma/\nu = 4000$ anti-parallel calculation. The D_m are ordered with lower-order D_m bounding higher-order D_m for all times. The periods of steepest growth at $t < 16$ and $t \approx 90$ are just before strongly nonlinear reconnection events. The inset shows D_m^{-2} for comparison with the Euler results.

Domain $L_x \times L_y \times L_z$	Label	Final mesh	Final time
$3\pi \times 3\pi \times 2\pi$	v11a	$1024 \times 512 \times 4096/8192$	$t = 13.75/14.25$
$4\pi \times 4\pi \times 2\pi$	v71	$1024 \times 512 \times 4096$	$t = 14.25$
$4\pi \times 4\pi \times 4\pi$	v11bx	$1024 \times 512 \times 4096$	$t = 14.25$
$4\pi \times 8\pi \times 2\pi$	v11bzz	$1024 \times 1024 \times 4096/8192$	$t = 14.25/15$
$4\pi \times 16\pi \times 2\pi$	v11g	$1024 \times 2048 \times 4096$	$t = 14.5$

TABLE 1. Some of the domains and sequences of meshes used to determine the role of the domain size upon growth. The extensions of the v11a and v11bzz calculations to $t = 14.25$ and $t = 15$ respectively, using $nz = 8192$, were used to test the convergence of higher-order Ω_m and the maximum of vorticity $\|\boldsymbol{\omega}\|_\infty$.

The original goal when these simulations were begun was to determine whether Euler calculations would show the same Navier–Stokes hierarchy, and from that gain insight into role of the nonlinearity in forming the new Navier–Stokes hierarchy. The interest comes from how the D_m hierarchy in figure 2 forms during the period of strong growth for $t < 16$, the time scale of the Euler calculations considered here. Before $t = 16$, when reconnection begins (Kerr 2013), viscous effects are negligible and the nonlinear (Euler) terms should dominate.

Would an Euler calculation show the same hierarchy? Figure 5 shows that it does for an extended period by plotting the squared inverses, the D_m^{-2}, without further rescaling. In this form, growth going as $(T_c - t)^{-1}$ appears as straight lines going to zero. Note that in this figure the lower orders are bounding from below.

However, there are signs in figure 5 that at late times the hierarchy is breaking down, and to address this question, new time-derivative diagnostics are introduced,

https://doi.org/10.1017/jfm.2013.325 Published online by Cambridge University Press

first to explain the trends in figure 5, and then to show convergence towards super-exponential growth. The importance of using all the Ω_m, or D_m, and their time derivatives is that the growth of $\sup|\boldsymbol{\omega}|$, by itself, is an inadequate test for distinguishing the type of growth.

3. Computational method, domain and new initial condition

All the calculations are, fundamentally, in periodic computational domains, with symmetries used to decrease the data and time needed to do the calculations. Of the several filtered/dealiased pseudospectral methods tested by Bustamante & Kerr (2008), the method chosen for the calculations here is a combination of the 2/3 dealiasing rule plus a 36th-order filtering that was first introduced without dealiasing (Hou 2008).

The axes are as follows: x is the direction of propagation of the vortex pair, y is in the primary direction of the vortices, and z is the direction between the vortices. The computed domain size is $L_x \times L_y \times L_z$, while the fully periodic domain would be in $L_x \times 2L_y \times 2L_z$. Domain sizes and meshes are given in table 1. Referring to figure 8, the $y = 0$ symmetry plane with the maximum perturbation will be the *perturbation plane* and the $z = 0$ symmetry plane between the vortices will be the *dividing plane*.

Initial condition. At a meeting on the Euler equations in 2007 in Aussois, France, the conclusions on regularity of the two anti-parallel calculations given (Bustamante & Kerr 2008; Hou 2008) were different, even though both used initial conditions based on Kerr (1993). The flaws in the Kerr (1993) prescription have now been identified and corrected.

The three new elements of the initial condition are as follows.

(i) A new vorticity profile for the core based upon the Rosenhead regularization of a two-dimensional point vortex $|\boldsymbol{\omega}|(r) = \Gamma\ a^2/(r^2 + a^2)^2$ with a radius of $a = 0.75$.

(ii) A new vorticity direction algorithm that, for a given (x_i, y_j, z_k) on the three-dimensional grid, begins by finding the two nearest positions on the prescribed analytic trajectory (x_s, y_s, z_s). The tangent between these two nearest points is used to define $r = |(x_i, y_j, z_k) - (x_s, y_s, z_s)|$, the distance used in the profile function for $|\boldsymbol{\omega}|(x_i, y_j, z_k)$, and to define the direction of the vorticity $\hat{\boldsymbol{\omega}} = \boldsymbol{\omega}/|\boldsymbol{\omega}|$ at the grid points (x_i, y_j, z_k). The resulting variation of the initial circulation in y-planes, $\Gamma(y)$ is 1 %.

(iii) The very long perturbed trajectory from Kerr (2011):

$$(x, y, z)(y) = (\delta_x[2/\cosh([y/\delta_y]^{1.8}) - 1], y, 0).$$

These steps are applied on a modest mesh, then a $\exp(-0.01k^4)$ hyperviscous filter is applied and finally this field is remeshed onto a much larger computational mesh by adding zeros at the higher wavenumbers, zeros that blend into the filter at large k. Additional remeshings are applied as the structures collapse to ever smaller scales until, eventually, the limits of machine resolution are reached.

The new trajectory is shown in figure 1, with the inset of the upper/left quarter domain near the $y = 0$ perturbation plane, showing that the initial vortex tube has a circular cross-section of constant width along its entire length. Variations upon these initial vortices have been used for vertical vortices in a stratified fluid, the anti-parallel unstratified Navier–Stokes calculations mentioned here, and the new anti-parallel Euler vortices. In each case, unphysical initial instabilities do not appear.

Following previous work (Kerr 1993; Bustamante & Kerr 2008; Hou 2008), all of the calculations used anisotropic meshes, with most taking $\Delta z = 2\Delta x = 4\Delta y$.

https://doi.org/10.1017/jfm.2013.325 Published online by Cambridge University Press

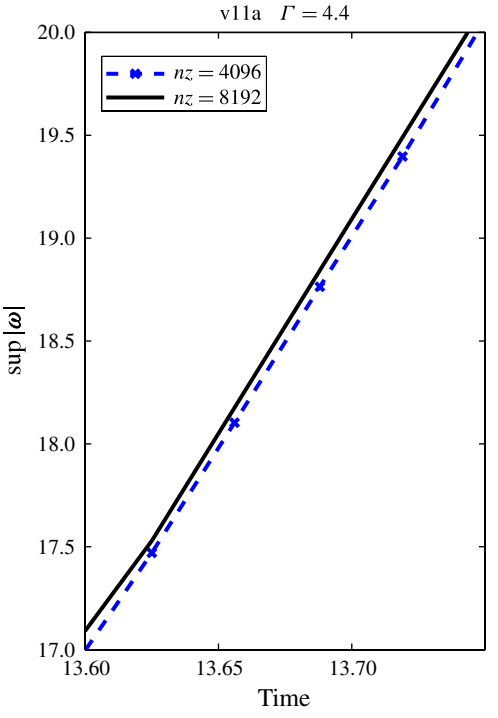


FIGURE 3. Comparison of sup $|\boldsymbol{\omega}|$ for case v11a for $nz = 4096$ and $nz = 8192$. The convergence of these two calculations up to $t = 13.75$ sets the minimum distance z_∞ of sup $|\boldsymbol{\omega}|$ from the x–y dividing plane.

Fine resolution is most critical in z due to the flattening of the vortices, with the requirement that the z-position of sup $|\boldsymbol{\omega}(t)|$, z_∞ be more than 12 mesh points from the $z = 0$ dividing plane for sup $|\boldsymbol{\omega}(t)|$ to converge. While this is confirmed by figure 3, where the mesh in z for case v11a has been doubled, all of the higher-order Ω_m emphasized here converge upon remeshing as long as $z_\infty > 8\Delta z$. Remeshes were done when $z_\infty \approx 24\Delta z$. Following the example in Bustamante & Kerr (2008), the other check on accuracy was to follow the circulation $\Gamma(y)$ of each y-plane. This is maintained to order 10^{-4}.

Several large calculations were run to identify a domain for which the boundaries were not the source of any relaxation of the growth of the maximum of vorticity $\|\boldsymbol{\omega}\|_\infty$. These tests found that changing the length of the domain in the y-direction had the greatest effect upon growth, with case v11bzz with $L_y = 8\pi$ being the smallest domain that satisfies this criterion.

To demonstrate consistency with earlier calculations, figure 4 plots sup $|\boldsymbol{\omega}|^{-1}$, z_∞ and Z_p^{-1} (2.2), all of which went as $T_c - t$ in Kerr (1993), and do here as well with a common $T_c \approx 15$–16 at first glance. However, appearances can be deceiving and the goal here is to supersede the old sup $|\boldsymbol{\omega}|^{-1}$ and Z_p^{-1} tests.

4. Rescaled vorticity moments from the Euler calculations

That Kerr (1993) found sup $|\boldsymbol{\omega}| \approx \|\boldsymbol{\omega}\|_\infty \sim (T_c - t)^{-1}$ was anticipated as this is consistent with the lower bound for singular power-law growth allowed by the

https://doi.org/10.1017/jfm.2013.325 Published online by Cambridge University Press

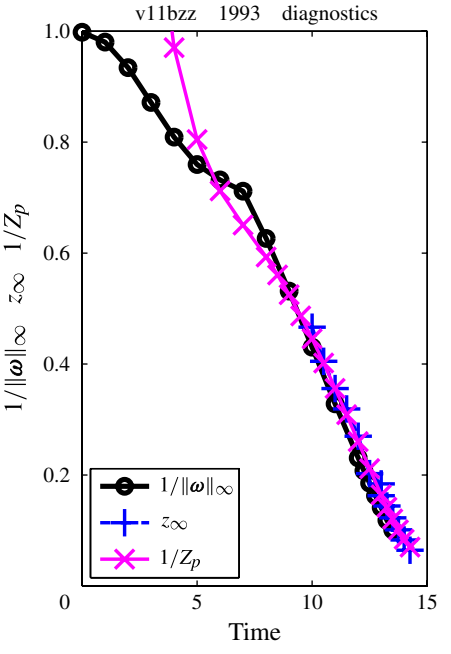


FIGURE 4. For case v11bzz, the singular diagnostics used in Kerr (1993). $\|\boldsymbol{\omega}\|_\infty^{-1}$, z_∞ and $Z_p^{-1} = \mathrm{d}Z/\mathrm{d}t$, the production of enstrophy. All decrease approximately linearly towards zero.

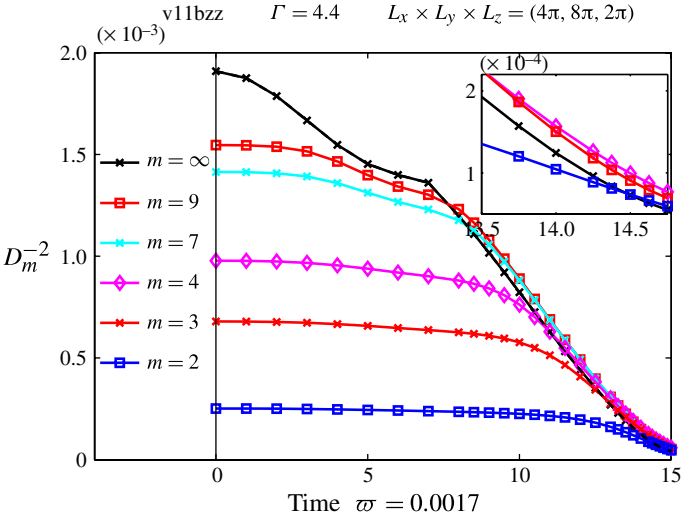


FIGURE 5. The inverses: $D_m^{-2}(t)$ for case v11bzz. The approach to a common linear decrease for $m > 1$ represents strong, convergent growth in all the D_m as $t \to 15.8$. The hierarchy of $D_m^{-2}(t)$ includes $\varpi/\|\boldsymbol{\omega}\|_\infty$. The inset shows the D_m^{-2} crossing for large m, which is not seen for the large m Navier–Stokes D_m^{-2} in the inset of figure 2.

https://doi.org/10.1017/jfm.2013.325 Published online by Cambridge University Press

Beale *et al.* (1984) test. However, finding $Z_p \sim (T_c - t)^{-1}$ implies that $Z \sim D_1 \sim \log(T_c - t)$, which was unexpectedly small growth.

The ability to look at all the vorticity moments will now be used to close that gap. The conclusions will be that in the context of the new hierarchy, even though $\sup|\boldsymbol{\omega}| \sim (T_c - t)^{-1}$ and $Z \sim \log(T_c - t)$ persist together for an extended period, this incompatibility is only resolved once all the moments converge to super-exponential growth.

The D_m Euler analysis for case v11bzz uses $\varpi_0 = \varpi_\Gamma = \Gamma/\mathsf{L}^2 = 0.0019$ with $\mathsf{L} = 2L_y$, the largest length scale in the problem. Figure 5 compares the D_m^{-2}, rather than the D_m as in figure 2, to show consistency with $\|\boldsymbol{\omega}\|_\infty^{-1} \sim D_\infty^{-2} \sim (T_c - t)$ in figure 4. Thus, the lower-order D_m^{-2} bound the nearly linear higher-order D_{m+1}^{-2} from below instead of lower-order D_m bounding the higher-order D_m from above as in figure 2.

What figure 5 shows is that for $m > 1$, all the D_m^{-2} appear to follow $D_m^{-2} \sim (T_c - t)$, with $m = 2$ joining the others near the final time calculated. However, note that for all $t > 9$, $\sup|\boldsymbol{\omega}|^{-1} < D_m$ for $m \geqslant 5$ and at the very last times, as highlighted by the inset, for large m the hierarchy has been broken, with $D_9^{-1} < D_3^{-1}$. Taken together, these two observation suggest that, despite first appearances, the growth rates of the D_m^2 are something less than $(T_c - t)^{-1}$. To address this question properly, more sensitive diagnostics will now be used. Note that in the lower inset of figure 2, the Navier–Stokes D_m^{-2} never cross during this period, even as the D_m^{-2} begin to increase.

4.1. *Using the D_m time derivatives*

If $\sup|\boldsymbol{\omega}| \approx \|\boldsymbol{\omega}\|_\infty$ were the only diagnostic for singular growth, then an appropriate secondary diagnostic would be $\alpha_\infty = \mathrm{d}\log\|\boldsymbol{\omega}\|_\infty/\mathrm{d}t$, the logarithmic time derivative of $\|\boldsymbol{\omega}\|_\infty$. However, to do this properly requires finding α_∞ at the exact position of $\|\boldsymbol{\omega}\|_\infty$ between the mesh points in physical space, which requires interpolation that can be difficult and inaccurate.

If the $\Omega_m \to \Omega_\infty$ as $m \to \infty$, using the Ω_m and their time derivatives $(\mathrm{d}/\mathrm{d}t)\Omega_m$, which have been determined at run-time, provides an alternative to finding α_∞, without the difficulties of interpolation. The $\mathrm{d}D_m^{-2}/\mathrm{d}t$ can also compared with an upper bound using the following new inequality.

One starts by following proof of Proposition 1 in Gibbon (2013),

$$2mL^3\Omega_m^{2m-1}\frac{\mathrm{d}}{\mathrm{d}t}\Omega_m \leqslant 2mL^3 c_{1,m}\Omega_{m+1}^{m+1}\Omega_m^m, \tag{4.1}$$

which, with some rearranging, becomes

$$\frac{\mathrm{d}}{\mathrm{d}t}\Omega_m \leqslant c_{1,m}\left(\frac{\Omega_{m+1}}{\Omega_m}\right)^{m+1}\Omega_m^2. \tag{4.2}$$

Finally, upon substituting the definition of the D_m and pulling the ϖ_0 out, one gets

$$\frac{\mathrm{d}}{\mathrm{d}t}D_m \leqslant 2c_{2,m}\varpi_0\left(\frac{D_{m+1}}{D_m}\right)^{\xi_m}D_m^3 \quad \text{where } \xi_m = \frac{1}{2}(4m+1), \tag{4.3}$$

which can be rewritten as

$$-\frac{\mathrm{d}}{\mathrm{d}t}D_m^{-2} \leqslant c_{2,m}\varpi_\Gamma\left(\frac{D_{m+1}}{D_m}\right)^{\xi_m}. \tag{4.4}$$

https://doi.org/10.1017/jfm.2013.325 Published online by Cambridge University Press

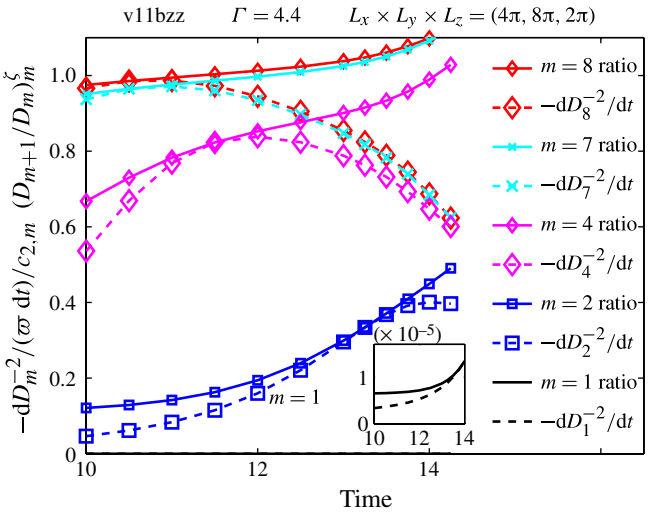


FIGURE 6. Comparison using (4.4) of $\mathrm{d}D_m^{-2}/\mathrm{d}t(c_{2,m}\varpi_\Gamma)^{-1}$ to $(D_{m+1}/D_m)^{\xi_m}$ for case v11bzz. Bounds given by (4.4) are followed for $t < 11$. For $t > 11$, $(D_{m+1}/D_m)^{\xi_m}$ rises above 1 and $\mathrm{d}D_m^{-2}/\mathrm{d}t$ diverges from this bound for large m.

When expressed in this way, the right-hand side contains only ratios of the D_m and the left-hand side contains only the time derivative of D_m^{-2}. However, because the power inside the $\mathrm{d}/\mathrm{d}t$ is negative, this inequality is not an upper bound on the $\mathrm{d}D_m/\mathrm{d}t$.

Instead, (4.4) provides a basis for comparing the $-\mathrm{d}D_m^{-2}/\mathrm{d}t$ with their ratios, ratios that are converging to constants. So if the $-\mathrm{d}D_m^{-2}/\mathrm{d}t$ follow their upper bounds, this could explain what drives the phase where the $D_m^{-2} \sim (T_c - t)$. And if the $-\mathrm{d}D_m^{-2}/\mathrm{d}t$ fall away from these upper bounds, one would expect some type of non-singular growth.

To make the comparison between the left-hand and right-hand sides of (4.4) complete, estimates for $c_{2,m}$ coefficients are needed. For the purposes here, the following maxima are used: $c_{2,m} = \max\,(D_{m+1}/D_m)^{\xi_m}/(-\mathrm{d}D_m^{-2}/\mathrm{d}t)$. Given these $c_{2,m}$, figure 6 compares the $-(\mathrm{d}D_m^{-2}/\mathrm{d}t)/(\varpi_\Gamma c_{2,m})$ and $(D_{m+1}/D_m)^{\xi_m}$, with $m = 2, 4, 7$ and 9 in the main plot and $m = 1$ in the lower right inset. The two goals are to determine how the ratios D_{m+1}/D_m change in time and when the $-\mathrm{d}D_m^{-2}/\mathrm{d}t$ follow their upper bounds – and when not.

The comparisons can be split into two phases, first for $t < 11$, when the higher-order ($m = 4, 7, 9$) ratios converge as $D_{m+1}/D_m \nearrow 1$, although not as rapidly as figure 5 would suggest. During this phase the $-\mathrm{d}D_m^{-2}/\mathrm{d}t/(\varpi_\Gamma c_{2,m})$ track the $(D_{m+1}/D_m)^{\xi_m}$ upper bounds, which could strengthen the new hierarchy and the $D_m^{-2} \sim (T_c - t)$ growth.

For $t > 11$ the situation changes as the new hierarchy is gradually broken, with the $(D_{m+1}/D_m)^{\xi_m}$ creeping above 1 for large m. This is consistent with how the D_m^{-2} cross in the inset of figure 5. In addition, the higher-order $-\mathrm{d}D_m^{-2}/\mathrm{d}t$ are diverging from their upper bounds to smaller values, pointing towards slower growth than the $(T_c - t)^{-1}$ power laws suggested by figure 5. Note that for $m = 1$, both D_2/D_1 and $-\mathrm{d}D_1^{-2}/\mathrm{d}t$ are growing rapidly, pointing to a time when D_1 might converge towards the $m > 1$ behaviour.

Figure 7 plots both $\log(\mathrm{d}\log\Omega_m/\mathrm{d}t)$ and $\log(\log\Omega_m)$ up to $t = 15$, when $z_\infty = 15\Delta z$ for $nz = 8192$. This shows that the slower growth indicated in figure 6 is super-

https://doi.org/10.1017/jfm.2013.325 Published online by Cambridge University Press

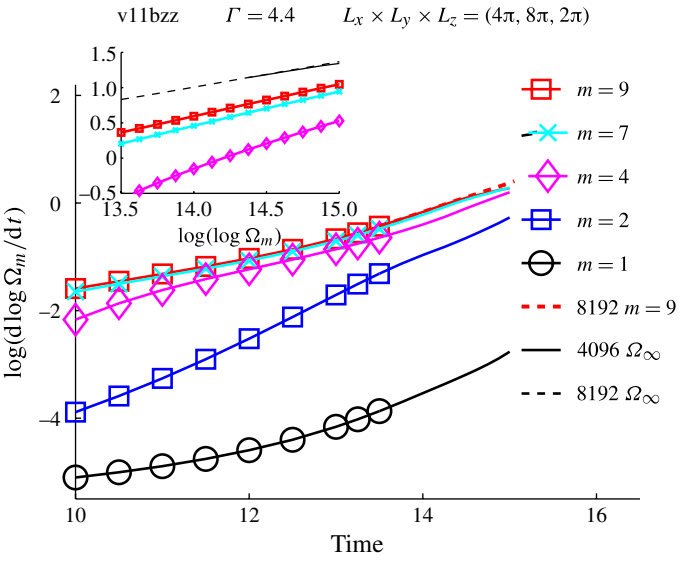


FIGURE 7. Plotting $\log(\mathrm{d}\log\Omega_m/\mathrm{d}t)$ shows that all of the Ω_m are asymptoting to super-exponential growth $\exp(\exp(a_m t))$ with $a_m \to 0.357 \pm 0.02$. The inset shows some late time, large m, $\log\log\Omega_m$, including $m = \infty$. Very late times show the two largest nz as a check on resolution effects.

exponential of the form $\Omega_m \to a_{1,m}\exp(a_{2,m}\exp(a_m t))$ for all m, including $m = \infty$, with the a_m all converging to a common value. How the different $\log(\mathrm{d}\log\Omega_m/\mathrm{d}t)$ converge towards a common $a_m t$ growth for $t \leqslant 13$ represents the transition from the $D_m^2 \sim (T_c - t)^{-1}$ phase to the final super-exponential phase.

Identical behaviour is observed for all the calculations in shorter domains, except the following combination as L_y is decreased: during the first phase the initial growth is stronger, the z_∞ collapse faster and the estimated singular times are later.

5. Three-dimensional images

To get suggestions for what drives the initial power-law growth, then inhibits it, figure 8 provides three-dimensional renderings of the vorticity at two late times, $t = 13.25$ and $t = 14.25$, from the v11bx calculation. The $y > 0$ half-domain highlights the growth of curvature in the bulge, then the growth in the divergence of the vortex lines. It is a kinematic requirement (Deng, Hou & Yu 2005) that the integral of the divergence of the vorticity direction $\int \mathrm{d}s\nabla\cdot\hat{\boldsymbol{\omega}}$ blows up if $\|\boldsymbol{\omega}\|_\infty$ blows up. It is also possible that large values of $\nabla\cdot\hat{\boldsymbol{\omega}}$, where $\hat{\boldsymbol{\omega}} = \boldsymbol{\omega}/|\boldsymbol{\omega}|$, could be what inhibits the growth of $\|\boldsymbol{\omega}\|_\infty$.

These figures can be compared with a similar stage ($t = 1.25$) in the evolution of anti-parallel quantum vortices in Kerr (2011) and to the cover illustration from Kerr (1996), which shows how the vortex lines twist as they extend from the anti-parallel interaction. What happens just after this configuration reconnects in Navier–Stokes calculations can be found in Kerr (2013).

Several isosurfaces and types of vortex lines are given for each time, with all the vortex lines originating at points on the $y = 0$ perturbation plane. The trajectories were identified by applying the streamline function in MATLAB to the full vorticity vector

https://doi.org/10.1017/jfm.2013.325 Published online by Cambridge University Press

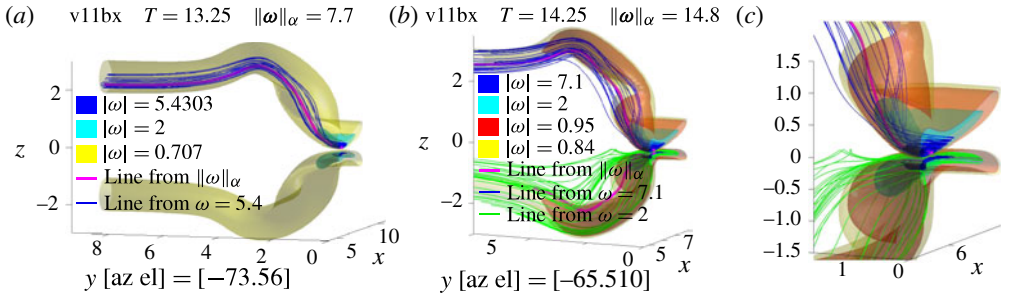


FIGURE 8. Isosurfaces and vortex lines in the $y > 0$ half-domain, where the $\pm z$ vortices are mirror images. Thick magenta lines originate at $\sup|\boldsymbol{\omega}|$. Yellow outer isosurfaces show the overall envelope. Blue isosurfaces show the region immediately around $\|\boldsymbol{\omega}\|_\infty$. (*a*) $t = 13.25$ with three isosurfaces. Two show the structure around $\|\boldsymbol{\omega}\|_\infty$. The outer envelope surface shows how the strongly interacting region near $y = 0$ connects to the original vortices, with some twist along the way. The blue vortex lines coming from the $|\boldsymbol{\omega}| = 0.7\|\boldsymbol{\omega}\|_\infty$ isosurface stay bundled, except for some divergence when they cross $y = 2$. (*b,c*) $t = 14.25$, showing four isosurfaces with more twist and distortion. Two surfaces represent the innermost region, an intermediate surface (red) is the most convoluted, plus the yellow envelope surface. The inner vortex lines (magenta and blue) remain bundled, with more spreading than at $t = 13.25$. The isosurfaces are most convoluted near $y = 2$. The green vortex lines, originating on the $y = 0$, $|\boldsymbol{\omega}| = 2$ isosurface, are more spread out and twisted than the inner lines, with a twist that brings one close to the $z = 0$ dividing plane near $y = 2$, which could enhance the local stretching rate.

fields. The thick (magenta) lines originate at interpolated positions between the mesh points with the absolute maxima of the vorticity. The multiple, thinner blue and green lines originate from points where the blue and cyan inner isosurfaces, respectively, cross the $y = 0$ perturbation plane.

For both times, an outer, yellow isosurface is used to show how the envelope of the vortices evolves. For $t = 13.25$, note how the outer isosurface for $z < 0$ twists about itself for $1 \leqslant |y| \leqslant 2$ and there is strong curvature in a bulge for $2 \leqslant |y| \leqslant 4$. The stretching of vorticity on the $y = 0$ perturbation plane is induced by this bulge, which sits roughly where the periodic boundary in y would be if a domain with $L_y = \pi$ were used. To get the strong stretching and the power-law phase observed here, $L_y > 2\pi$ is needed.

The strongest velocity is in a jet that goes from right to left through the gap between the vortices on the $y = 0$ perturbation plane. This jet is responsible for a build-up in vorticity at the leading edge and the $y = 0$ head–tail (left–right) configuration for the highest two isosurfaces, cyan ($|\boldsymbol{\omega}| = 2$) and dark blue ($\sim 0.5\|\boldsymbol{\omega}\|_\infty$). The curvature of the vortices at $y = 0$ is small for both times, consistent with the flatness of the isosurfaces. Strong curvature and divergence of the vortex lines starts at $y \approx 1$.

The divergence $\boldsymbol{\nabla} \cdot \hat{\boldsymbol{\omega}}$, is greatest at $y \approx 2$, where there is some twist to the outer isosurface for $t = 13.25$ and a strong pinch of the $|\boldsymbol{\omega}| = 0.95$ isosurface at $t = 14.25$, a pinch because the divergence weakens $|\boldsymbol{\omega}|$ in this region.

For both times, the large, growing bulges to large $\pm z$ at $y \approx 3$ bend back towards the $z = 0$ dividing plane for $4 \leqslant y \leqslant 6$. In two recent vortex reconnection calculations, viscous (Kerr 2013) and quantum (Kerr 2011), this back bend overshoots the original z level of the vortices, leading to a second reconnection site, additional vortex stretching and the formation of vortex rings.

https://doi.org/10.1017/jfm.2013.325 Published online by Cambridge University Press

6. Summary

A new approach using all the vorticity moments has been applied to the analysis of new Navier–Stokes and Euler calculations. The advantage of using the rescaled D_m and the volume-averaged Ω_m moments in numerical analysis is that their values, time derivatives, and thus their logarithmic times derivatives, can be determined continuously in time and be compared.

When the viscous D_m analysis was first applied to the Navier–Stokes anti-parallel vortex reconnection data using the new initial condition, the unexpected D_m hierarchy shown in figure 2 was found. In this hierarchy, each lower-order D_m bounds the higher-order D_{m+1} for all times and all of the Navier–Stokes calculations mentioned – an ordering opposite to the Hölder ordering of the Ω_m.

The Euler calculations in this paper were run to examine how much of this hierarchy would appear if $\nu = 0$. Initially, up to $t = 13$, the $D_m \geqslant D_{m+1}$ hierarchy is reproduced for $m < \infty$, and, except for $m = 1$, all the $D_m^{-2} \sim c_m(T_m - t)$ with roughly the same coefficients c_m and estimated singular times T_m.

This power-law phase is stronger and lasts longer when the y-domain dimension L_y is larger, indicating that an overly confined geometry would inhibit growth, possibly by suppressing the type of curvature growth seen in the formation of the bulges in figure 8, which would in turn inhibit the non-local Biot–Savart vortex stretching terms. This could be why this phase is not seen in anti-parallel calculations with smaller y-domains.

Next, by using more precise time-derivative analysis, it is shown that the power-law phase and the $D_m \geqslant D_{m+1}$ hierarchy eventually breaks down. The final analysis of the logarithmic time derivatives shows that following the transition, a second phase develops during which all the Ω_m are converging towards the same super-exponential growth. During this phase, there is strong growth in the divergence of the vortex lines in figure 8. Accommodating this growth in the divergence could be what is inhibiting the initial power-law growth of the D_m.

While the final Euler phase breaks the $D_m \geqslant D_{m+1}$ hierarchy that originally formed, the inset in figure 2 shows that during this period the Navier–Stokes D_m hierarchy is preserved, even though the growth of the D_m is reversed. This indicates, first the importance of the viscous terms in preserving the new D_m hierarchy once it has formed, and second, that the initial power-law phase, even if this is not the final, asymptotic growth, contains the Euler dynamics most relevant for the generation of the new hierarchy in Navier–Stokes solutions.

Initial tests show that these calculations have the resolution needed for quantifying the growth of the curvature and divergence on the vortex lines (Deng *et al.* 2005). This should be on more than one line since the maximum curvature in figure 8 appears on lines that start near, but not at, $\|\boldsymbol{\omega}\|_\infty$. Then new simulations are needed that will look at tighter initial distributions of vorticity, either vortex sheets or thinner vortex tubes, to give us new ideas for what the origin of the power-law phase might be.

Acknowledgements

The author thanks the Isaac Newton Institute and the organizers of IUTAM Symposium Topological Fluid Dynamics II, 23–27 July 2012 for the invitation to participate. I thank J. D. Gibbon for supporting discussions and mathematics and advice from an anonymous reviewer on the use of (4.4). Computing support was provided by the Warwick Centre for Scientific Computing.

https://doi.org/10.1017/jfm.2013.325 Published online by Cambridge University Press

References

BEALE, J. T, KATO, T. & MAJDA, A. 1984 Remarks on the breakdown of smooth solutions of the 3-D Euler equations. *Commun. Math. Phys.* **94**, 61–66.

BUSTAMANTE, M. D. & KERR, R. M. 2008 3D Euler about a 2D symmetry plane. *Physica* D **237**, 1912–1920.

DENG, J., HOU, T. Y. & YU, X. 2005 Geometric properties and nonblowup of 3D incompressible Euler flow. *Comm. Part. Diff. Equ.* **30**, 225–243.

DOERING, C. R. 2009 The 3D Navier–Stokes problem. *Annu. Rev. Fluid. Mech.* **41**, 109–128.

DONZIS, D., GIBBON, J. D., KERR, R. M., PANDIT, R., GUPTA, A. & VINCENZI, D. 2013 Rescaled vorticity moments in the 3D Navier–Stokes equations. *J. Fluid Mech.* (submitted), arXiv:1302.1768.

GIBBON, J. D. 2012 Conditional regularity of solutions of the three-dimensional Navier–Stokes equations and implications for intermittency. *J. Math. Phys.* **53**, 115608.

GIBBON, J. D. 2013 Dynamics of scaled norms of vorticity for the three-dimensional Navier–Stokes and Euler equations. *Procedia IUTAM* **7**, 49–58.

HOU, T. Y. 2008 Blow-up or no blow-up? The interplay between theory and numerics. *Physica* D **237**, 1937–1944.

KERR, R. M. 1993 Evidence for a singularity of the three-dimensional, incompressible Euler equations. *Phys. Fluids* A **5**, 1725–1746.

KERR, R. M. 1996 Cover illustration: vortex structure of Euler collapse. *Nonlinearity* **9**, 271–272.

KERR, R. M. 2011 Vortex stretching as a mechanism for quantum kinetic energy decay. *Phys. Rev. Lett.* **106**, 224501.

KERR, R. M. 2012 Dissipation and enstrophy statistics in turbulence: are the simulations and mathematics converging? *J. Fluid Mech.* **700**, 1–4.

KERR, R. M. 2013 Swirling, turbulent vortex rings formed from a chain reaction of reconnection events. *Phys. Fluids* **25**, 065101.

YEUNG, P. K., DONZIS, D. A. & SREENIVASAN, K. R. 2012 Dissipation, enstrophy and pressure statistics in turbulence simulations at high Reynolds numbers. *J. Fluid Mech.* **700**, 5–15.

https://doi.org/10.1017/jfm.2013.325 Published online by Cambridge University Press